ARCHIVE OF MECHANICAL ENGINEERING

DOI: 10.24425/ame.2026.1882 2026, Vol. 73, No. 3, pp. 405–428

Rina REORITA [1], Agus Yodi GUNAWAN [2], Novry ERWINA [2]

Thermal fluid flow in a porous rectangular cavity driven by differential heating and uniform heat fluxes

Received 17 December 2025, **Revised** 1 May 2026, **Accepted** 24 May 2026, **Published online** 6 July 2026

Keywords: natural convection, porous medium, Boussinesq approximation, asymptotic solution, finite-difference method

This paper investigates the complex dynamics of thermal fluid flow within a porous rectangular cavity, subjected to a hybrid thermal environment consisting of differential heating on the top wall and uniform heat fluxes on the vertical boundaries. The study aims to characterize the interaction between buoyancy-driven convection and localized heat input within a saturated porous medium, modeled using the Darcy model. The governing equations are described by the continuity equation, the momentum equation, and the energy equation. The equations were made dimensionless. Three dimensionless parameters are introduced, namely the Darcy-Rayleigh number (the porous medium conductivity parameter), the heat flux parameter, and the geometric aspect ratio (the cavity shape parameter). Numerical solutions were conducted by using the finite-difference method. Special attention is paid to finding an analytical solution for a small Darcy-Rayleigh number by using the asymptotic expansion method. Our simulation results show that the interaction between these boundary conditions creates complex, multi-cellular flow patterns and directly impacts heat transfer efficiency, offering insights for thermal management applications. Furthermore, the study provides a comprehensive mapping of the temperature distribution and streamline patterns, offering critical insights into heat transfer optimization.

✉ Agus Yodi GUNAWAN, email: ayodi@itb.ac.id

[1]Doctoral Program of Mathematics, Faculty of Mathematics and Natural Sciences, Institut Teknologi Bandung, Jl. Ganesha, 10, Bandung, 40132, West Java, Indonesia. Email: 30122002@mahasiswa.itb.ac.id,

[2]Department of Mathematics, Faculty of Mathematics and Natural Sciences, Institut Teknologi Bandung, Jl. Ganesha, 10, Bandung, 40132, West Java, Indonesia.

© 2026. The Author(s). This is an open-access article distributed under the terms of the Creative Commons Attribution (CC-BY 4.0, https://creativecommons.org/licenses/by/4.0/), which permits use, distribution, and reproduction in any medium, provided that the author and source are cited.

1. Introduction

The thermal fluid flow in a porous medium has been extensively explored by researchers across scientific and technological disciplines [1–3]. This topic has become particularly significant due to the rise of porous insulation technologies, gas-cooled electric machines, nuclear reactors, and geothermal reservoir zones [4, 5]. The increasing focus on flow in a porous medium underscores its practical relevance and emphasizes its applicability in real-world scenarios.

Porous medium in a confined cavity inevitably affects heat distribution. As stated in Kang et al. [6], the heat transfer mechanisms in a porous medium are thermal conduction along its solid matrix, thermal radiation across internal pores, and conduction through fluid filling the pores. In a permeable porous medium, the heat distribution can be further increased by natural convection [7].

Heat distribution in a confined porous cavity depends on two essential aspects: the fluid type and the geometry of the domain. Newtonian fluids are the most common in daily life and thus the most widely discussed by researchers [8–11]. The geometry of the domain also significantly influences heat transfer, which is crucial for calculating energy consumption [12]. Some theoretical studies were conducted in two-dimensional domains, rather than three-dimensional. Although the three-dimensional domain can better describe the actual phenomenon, research in this area is still in its infancy due to its high costs and complicated computing [13]. Moreover, Botton et al. [14] produced good approximation results for the temperature field in the two-dimensional domain, allowing the solidification problem of metal liquids discussed in the research to be regarded as a two-dimensional problem.

Natural convection in a two-dimensional porous medium, particularly in rectangular cavities, is a fundamental area of study. Yang et al. [15] outlined three classical models for analyzing natural convection in rectangular domains: the Rayleigh–Bénard convection, vertical convection, and horizontal convection. The Rayleigh–Bénard convection occurs when the cavity is heated from the bottom and cooled from the top. Vertical convection occurs when the cavity is heated on one vertical wall and cooled on the opposite wall. Horizontal convection occurs when the cavity is heated and cooled at one horizontal side simultaneously [16].

Horizontal convection occurs in various phenomena. In groundwater systems, uneven heating of the Earth's surface and heat flows are influenced by local heat sources such as magma chambers in the caldera [17]. In industrial settings, such as glass furnaces, horizontal convection is essential [18]. Temperature variations create convective currents that facilitate the even melting and mixing of the glass material. Furthermore, horizontal convection can be observed in stratified fluid systems in lakes, oceans, and atmospheres [19].

In addition to numerical investigations of natural convection within porous enclosures, various analytical and semi-analytical studies have been conducted by researchers. Walker and Homsy [20] employed asymptotic methods to describe

convection in a porous cavity. The boundary layer analysis of vertical porous enclosures and the analytical-numerical examination of shallow porous cavities were investigated by Bejan [21]. Daniels and Punpocha [22], in a study relevant to our present work, studied the boundary-layer structure and asymptotic behavior of differentially heated cavity flow in porous media. They established the theoretical foundation for understanding the influence of cavity geometry, the Darcy-Rayleigh number, and the thermal boundary conditions on flow and heat transfer.

Many studies have considered horizontal convection in rectangular cavities with varying temperature profiles on the boundaries. Yang et al. [15] conducted numerical analyses of thermal fluid behavior driven by a linear temperature profile at the bottom of the non-porous cavity, with the side and top walls being thermally insulated. Sheard and King [23] completed a comparable study, which highlighted the scaling of the mean Nusselt number and boundary-layer quantities in relation to the aspect ratio and Rayleigh number. Both Hossain et al. [24] and Yan and He [25], explored the effect of a linear temperature profile in shallow cavities. Chiu-Webster et al. [18] examined the flow of a highly viscous fluid driven by a linear temperature function at the top boundary, rather than the bottom. Tsai et al. [26] performed a different study, investigating the temperature profile at the bottom boundary based on a power function. Daniels [27] further modified horizontal convection in a porous medium, assuming that the temperature profile on the upper surface is a monotonic function. This condition resulted in a horizontal boundary-layer structure near the upper surface. Nevertheless, the absence of heat flux at the vertical walls in all the studies mentioned above presents a significant issue.

In the present work, we study the horizontal convection inspired by the work of Daniels and Punpocha [28]. As the novelty of the present study, we apply uniform heat fluxes on the vertical sides rather than thermally insulating them. From the perspective of thermal-insulation engineering, this model is not merely a theoretical concept but also a practical tool that can be utilized in real-world situations. In practice, the isothermal side walls do not resemble fibrous and granular insulation layers, especially in building technology. Therefore, the heat distribution along the vertical wall surface is more natural and resembles a state of uniform heat flux [29].

The paper is organized as follows. The mathematical model is formulated in Section 2 in terms of a stream function and temperature. The asymptotic solution to the small Darcy-Rayleigh number is presented in Section 3. Here, we also perform a numerical discretization using the finite-difference method. We then discuss the errors to validate our numerical computations in this chapter. Our numerical simulations are demonstrated in Section 4. Our conclusions are presented in the last section.

2. Mathematical formulation

In this chapter, we first derive a flow model of thermal fluid in a homogeneous and isotropic porous rectangular domain. Equations are governed by the continu-

ity, the momentum, and the energy equations. The dimensional analysis is then presented.

2.1. The model

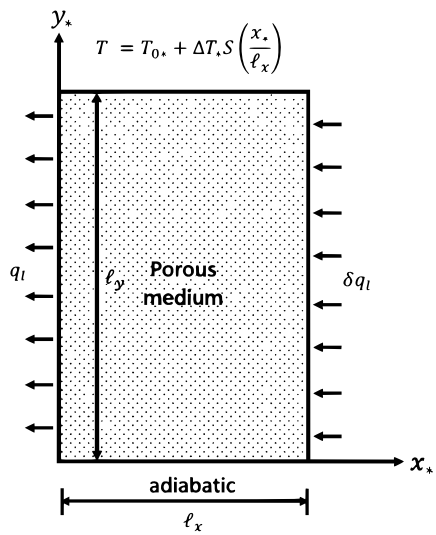

Fig. 1. A schematic diagram of our system

We investigate the flow of thermal fluid in a rectangular porous cavity $\{0 \leq x_* \leq \ell_x, 0 \leq y_* \leq \ell_y\}$, as shown in Figure 1. The flow is driven by differential heating on the upper boundary, which is represented by

$$T_* = T_{0*} + \Delta T_* S\left(\frac{x_*}{\ell_x}\right),$$

where T_{0*} is the temperature reference, ΔT_* is the temperature difference at the top wall, and $S\left(\frac{x_*}{\ell_x}\right)$ is a monotonic function defined from $x_* = 0$ to $x_* = \ell_x$. The bottom wall is assumed to be adiabatic. These boundary conditions are proposed by Daniels and Punpocha [28]. For the vertical walls, we propose the Neumann conditions, which transfer heat by uniform heat fluxes as follows:

$$k\left(\frac{\partial T_*}{\partial x_*}\right)_{x_*=0} = q_l \quad \text{and} \quad k\left(\frac{\partial T_*}{\partial x_*}\right)_{x_*=\ell_x} = \delta q_l,$$

where k is the thermal conductivity of a fluid-saturated porous medium. The constant δ describes the heat flux ratio between the left-side wall and the right-side one. It can be either negative or positive value, representing the incoming or outgoing flux at the wall.

The porous medium is assumed to be homogeneous and isotropic. The area-averaged fluid velocity through a column of porous matrix is assumed to satisfy the Darcy's law. Referring to Bejan [4], the related steady-state equations can be expressed as follows:

$$\frac{\partial u_*}{\partial x_*} + \frac{\partial v_*}{\partial y_*} = 0, \tag{1}$$

$$\frac{\mu}{K} u_* = -\frac{\partial p_*}{\partial x_*}, \tag{2}$$

$$\frac{\mu}{K} v_* = -\frac{\partial p_*}{\partial y_*} - \rho g, \tag{3}$$

$$u_* \frac{\partial T_*}{\partial x_*} + v_* \frac{\partial T_*}{\partial y_*} = \alpha \left(\frac{\partial^2 T_*}{\partial x_*^2} + \frac{\partial^2 T_*}{\partial y_*^2} \right). \tag{4}$$

Here u_* and v_* represent the velocity components corresponding to the coordinates x_* and y_*, respectively, p_* represents the pressure, and K represents the permeability of the porous medium. The parameters μ, g, ρ, and α denote the absolute viscosity of the fluid, the gravitational acceleration, the density of the fluid, and thermal diffusivity, respectively.

Applying the Boussinesq approximation to the momentum equation and cross-differentiating Equations (2) and (3) to eliminate the pressure term, we finally obtain the following governing equations:

$$\frac{\partial u_*}{\partial x_*} + \frac{\partial v_*}{\partial y_*} = 0, \tag{5}$$

$$\frac{\mu}{K} \left(\frac{\partial v_*}{\partial x_*} - \frac{\partial u_*}{\partial y_*} \right) = \rho_0 g \beta \frac{\partial (T_* - T_{0*})}{\partial x_*}, \tag{6}$$

$$u_* \frac{\partial T_*}{\partial x_*} + v_* \frac{\partial T_*}{\partial y_*} = \alpha \left(\frac{\partial^2 T_*}{\partial x_*^2} + \frac{\partial^2 T_*}{\partial y_*^2} \right), \tag{7}$$

where ρ_0 is the density reference and β is the thermal expansion coefficient.

To explore the flow field behavior, we introduce $\psi_*(x_*, y_*)$ as the stream function. The stream function provides the flow field, which is always tangential to the velocity of the fluid at every point along its length. By setting

$$u_* = \frac{\partial \psi_*}{\partial y_*} \quad \text{and} \quad v_* = -\frac{\partial \psi_*}{\partial x_*},$$

we can transform the governing equation into the following equations:

$$\frac{\mu}{K} \left(\frac{\partial^2 \psi_*}{\partial x_*^2} + \frac{\partial^2 \psi_*}{\partial y_*^2} \right) = -\rho_0 g \beta \frac{\partial (T_* - T_{0*})}{\partial x_*}, \tag{8}$$

$$\frac{\partial \psi_*}{\partial y_*} \frac{\partial T_*}{\partial x_*} - \frac{\partial \psi_*}{\partial x_*} \frac{\partial T_*}{\partial y_*} = \alpha \left(\frac{\partial^2 T_*}{\partial x_*^2} + \frac{\partial^2 T_*}{\partial y_*^2} \right). \tag{9}$$

Equations (8) and (9) are subject to following boundary conditions:

$$\psi_* = 0, \quad k\frac{\partial T_*}{\partial x_*} = q_l, \quad \text{on} \quad x_* = 0,$$
$$\psi_* = 0, \quad k\frac{\partial T_*}{\partial x_*} = \delta q_l, \quad \text{on} \quad x_* = \ell_x,$$
$$\psi_* = \frac{\partial T_*}{\partial y_*} = 0, \quad \text{on} \quad y_* = 0,$$
$$\psi_* = 0, \quad T_* = T_{0*} + \Delta T_* S\left(\frac{x_*}{\ell_x}\right), \quad \text{on} \quad y_* = \ell_y.$$

2.2. Dimensionless governing equations

To express the dimensionless governing equations, we apply the following scalings:

$$x = \frac{x_*}{\ell_y}, \quad y = \frac{y_*}{\ell_y}, \quad \psi = \frac{1}{\alpha}\psi_*, \quad T = \frac{T_* - T_{0*}}{\Delta T_*},$$

and obtain

$$\frac{\partial^2\psi}{\partial x^2} + \frac{\partial^2\psi}{\partial y^2} = -R\frac{\partial T}{\partial x}, \tag{10}$$
$$\frac{\partial\psi}{\partial y}\frac{\partial T}{\partial x} - \frac{\partial\psi}{\partial x}\frac{\partial T}{\partial y} = \frac{\partial^2 T}{\partial x^2} + \frac{\partial^2 T}{\partial y^2}. \tag{11}$$

The relevant boundary conditions are:

$$\psi = 0, \quad \frac{\partial T}{\partial x} = \eta_0 \quad \text{on} \quad x = 0, \tag{12}$$
$$\psi = 0, \quad \frac{\partial T}{\partial x} = \delta\eta_0 \quad \text{on} \quad x = L, \tag{13}$$
$$\psi = \frac{\partial T}{\partial y} = 0 \quad \text{on} \quad y = 0, \tag{14}$$
$$\psi = 0, \quad T = S\left(\frac{x}{L}\right) \quad \text{on} \quad y = 1. \tag{15}$$

In (10), R denotes the Darcy-Rayleigh number, which is defined by:

$$R = \frac{K\rho_0 g\beta\Delta T_*\ell_y}{\alpha\mu}. \tag{16}$$

In (12) – (15), $L = \ell_x/\ell_y$ is the geometric aspect ratio, and the parameter $\eta_0 = q_l\ell_y/(k\Delta T_*)$ is the dimensionless heat flux parameter.

Remark: It should be noted that the Darcy-Rayleigh number R reflects the balance between buoyancy, viscous resistance, and thermal diffusion. It does not directly measure inertial effects. Therefore, a large value of R as it appears in our discussion can be interpreted as a large value of ΔT_* (high temperature difference) inside a sparse porous medium. The applicability of the pure Darcy model at large R is more appropriately assessed using an inertial measure, such as the pore-scale or porous-medium Reynolds number [30]. Since the present study adopts the classical Darcy framework without inertial or Forchheimer corrections, interpretation of the results at higher R should take this limitation into account.

In the next chapter, we examine the asymptotic solution of the (10) – (11) with the boundary conditions (12) – (15) for a small Darcy-Rayleigh number, and the numerical simulation using the finite-difference method.

3. Method of solutions

In this chapter, we explore solutions of (10) – (15) using both asymptotic and numerical approaches. The asymptotic solution is constructed by assuming that the Darcy-Rayleigh number R is small. For a moderate value of R, we perform numerical treatments using the finite-difference method.

3.1. Asymptotic solution for a small Darcy-Rayleigh number

We apply the following perturbation expansion in powers of R to get an asymptotic solution for a small Darcy-Rayleigh number:

$$T(x, y) = T_0(x, y) + RT_1(x, y) + R^2T_2(x, y) + \ldots, \tag{17}$$

$$\psi(x, y) = R\psi_1(x, y) + R^2\psi_2(x, y) + \ldots. \tag{18}$$

Following the work of Daniels and Punpocha [28], the temperature profile in (15) is written as:

$$S\left(\frac{x}{L}\right) = \frac{1}{2}\left(1 - \cos\left(\frac{\pi x}{L}\right)\right), \quad 0 \le x \le L. \tag{19}$$

Remark: The cosine-based upper-wall temperature profile is selected to represent a smooth, monotonic nonuniform heating condition, indicating a gradual change in wall temperature along the top boundary. This approach avoids thermal boundary discontinuities and offers a physically plausible model of spatially graded heating. Such a situation may occur in practical systems involving porous insulation layers, solar-heated surfaces, geothermal formations, or enclosures subjected to nonuniform thermal loading. Additionally, it aligns well with our analytical method, as the solution is expressed via the Fourier series. Other smooth monotonic wall-temperature distributions may produce similar behavior because they

impose gradual thermal forcing. For the non-monotonic temperature profile (e.g., a convex-concave profile), it can alter the flow structure. We expect the multi-cell circulation will occur, since that case can be considered, at least, as two combinations of two domains having a monotonic temperature profile at each domain.

Substituting (17) and (18) in (10) and (11), we obtain the zeroth order term for $T(x, y)$ given by:

$$\frac{\partial^2 T_0}{\partial x^2} + \frac{\partial^2 T_0}{\partial y^2} = 0, \tag{20}$$

with boundary conditions:

$$\frac{\partial T_0}{\partial x} = \eta_0 \quad \text{on} \quad x = 0, \tag{21}$$

$$\frac{\partial T_0}{\partial x} = \delta\eta_0 \quad \text{on} \quad x = L, \tag{22}$$

$$\frac{\partial T_0}{\partial y} = 0 \quad \text{on} \quad y = 0, \tag{23}$$

$$T_0 = S\left(\frac{x}{L}\right) \quad \text{on} \quad y = 1. \tag{24}$$

Using the separation of variables method, we find the solution $T_0(x, y)$, as follows:

$$\begin{aligned} T_0(x, y) =& \frac{\eta_0 (1-\delta)}{2L}\left(y^2 - x^2 + \frac{1}{3}L^2 - 1\right) + \eta_0\left(x - \frac{1}{2}L\right) + \frac{1}{2} \\ &+ \left(-\frac{1}{2} - 2\eta_0 (1-\delta)\frac{L}{\pi^2} + 4\eta_0\frac{L}{\pi^2}\right)\operatorname{sech}\left(\frac{\pi}{L}\right)\cosh\left(\frac{\pi}{L}y\right)\cos\left(\frac{\pi}{L}\right) \\ &+ \sum_{n=2}^{\infty} 2\eta_0\left(\frac{L}{n^2\pi^2}\right)(1 - \delta(-1)^n)\operatorname{sech}\left(\frac{n\pi}{L}\right)\cosh\left(\frac{n\pi}{L}y\right)\cos\left(\frac{n\pi}{L}\right). \end{aligned} \tag{25}$$

For the first order term of ψ we get:

$$\frac{\partial^2 \psi_1}{\partial x^2} + \frac{\partial^2 \psi_1}{\partial y^2} = -\frac{\partial T_0}{\partial x}, \tag{26}$$

and supplemented by the following boundary conditions:

$$\psi_1 = 0 \quad \text{on} \quad x = 0, L, \tag{27}$$

$$\psi_1 = 0 \quad \text{on} \quad y = 0, 1. \tag{28}$$

Applying the same method as for the zeroth order $T_0(x, y)$, we obtain the solution $\psi_1(x, y)$ given by the following equation:

$$\begin{aligned}\psi_1(x,y) = &\left(C_1 \cosh\left(\frac{\pi}{L}y\right) + C_2 \sinh\left(\frac{\pi}{L}y\right) + 2\left(\frac{L^2}{\pi^3}\right)\eta_0\,(\delta+1)\right)\sin\left(\frac{\pi}{L}x\right)\\ &-\left(\frac{1}{4} + \eta_0\,(1-\delta)\,\frac{L}{\pi^2} - 2\eta_0\frac{L}{\pi^2}\right)\operatorname{sech}\left(\frac{\pi}{L}\right) y \sinh\left(\frac{\pi}{L}y\right)\sin\left(\frac{\pi}{L}x\right)\\ &+\sum_{n=2}^{\infty}\left\{\left[D_n \cosh\left(\frac{\pi}{L}y\right) + E_n \sinh\left(\frac{\pi}{L}y\right) + 2\left(\frac{L^2}{n^3\pi^3}\right)\eta_0\,(1-\delta(-1)^n)\right.\right.\\ &\left.\left.+\frac{\eta_0 L}{n\pi^2}\,(1-\delta(-1)^n)\operatorname{sech}\left(\frac{n\pi}{L}\right) y \sinh\left(\frac{n\pi}{L}y\right)\right]\sin\left(\frac{n\pi}{L}x\right)\right\},\end{aligned} \tag{29}$$

with:

$$C_1 = -2\eta_0\frac{L^2}{\pi^3}\,(\delta+1)\,,$$

$$C_2 = \frac{2\eta_0 L^2\,(\delta+1)}{\pi^3}\left(\coth\left(\frac{\pi}{L}\right) - \operatorname{csch}\left(\frac{\pi}{L}\right)\right) + \left(\frac{1}{4} + \frac{\eta_0\,(1-\delta)\,L - 2\eta_0 L}{\pi^2}\right)\operatorname{sech}\left(\frac{\pi}{L}\right),$$

$$D_n = -2\eta_0\frac{L^2}{n^3\pi^3}\,(1-\delta(-1)^n)\,,$$

$$E_n = \frac{2\eta_0 L^2}{n^3\pi^3}\,(1-\delta(-1)^n)\left(\coth\left(\frac{\pi}{L}\right) - \operatorname{csch}\left(\frac{\pi}{L}\right)\right) - \frac{\eta_0 L}{n\pi^2}\,(1-\delta(-1)^n)\operatorname{sech}\left(\frac{n\pi}{L}\right).$$

Next, we find $T_1(x, y)$ satisfying

$$\frac{\partial^2 T_1}{\partial x^2} + \frac{\partial^2 T_1}{\partial y^2} = \frac{\partial \psi_1}{\partial y}\frac{\partial T_0}{\partial x} - \frac{\partial \psi_1}{\partial x}\frac{\partial T_0}{\partial y}, \tag{30}$$

and in accordance with the following boundary conditions:

$$\frac{\partial T_1}{\partial x} = 0 \quad \text{on} \quad x = 0, L, \tag{31}$$

$$\frac{\partial T_1}{\partial y} = 0 \quad \text{on} \quad y = 0, \tag{32}$$

$$T_1 = 0 \quad \text{on} \quad y = 1. \tag{33}$$

Substituting T_0 and ψ_1 in Equations (25) and (29) to the right-hand side of (30), we obtain a Poisson equation with its right-hand side containing a Fourier series.

At this moment, we shall restrict ourselves to finding a solution to the first-order approximation of this Fourier series. After truncating the series and then applying the separation of variables method, we end up with the expression in the following equation:

$$\begin{aligned}
T_1(x,y) =& \frac{1}{2}Fy + \frac{1}{2}G + H_0\left[\left(C_1 - \frac{2L}{\pi}H_1\right)\sinh\left(\frac{\pi}{L}y\right) + \left(C_2 + \frac{1}{2}H_1 y\right)\cosh\left(\frac{\pi}{L}y\right)\right] \\
&- \frac{1}{32}H_1\left[\left(C_1 - \frac{L}{4\pi}H_1\right)\sinh\left(\frac{2\pi}{L}y\right) + \left(C_2 + \frac{1}{2}H_1 y\right)\cosh\left(\frac{2\pi}{L}y\right)\right] \\
&- \frac{1}{2}\sum_{n=2}^{\infty}\left\{\frac{L}{\pi^3}\eta_0\left(\delta(-1)^n - 1\right)H_n\left(\frac{\pi}{n}D_n + H_n - 2\right)\sinh\left(\frac{\pi}{L}y\right)\right. \\
&+ \frac{L}{n\pi^2}\eta_0\left(\delta(-1)^n - 1\right)\left(E_n + \frac{n}{L}H_n y\right)\cosh\left(\frac{\pi}{L}y\right) \\
&+ \frac{1}{4}\frac{n}{L}H_n K_n\left(\frac{n}{(n+1)^2}\cosh\left(\frac{(n+1)\pi}{L}y\right) - \frac{n}{(n-1)^2}\cosh\left(\frac{(n-1)\pi}{L}y\right)\right) \\
&- \frac{1}{4\pi}\frac{n^2}{(n+1)^2 L}H_n\left(2\frac{1-n}{n+1}H_n + \pi D_n\right)\sinh\left(\frac{2(n+1)\pi}{L}y\right) \\
&- \frac{1}{4\pi}\frac{n^2}{(n-1)^2 L}H_n\left(2H_n + \pi D_n\right)\sinh\left(\frac{2(n-1)\pi}{L}y\right) \\
&\left.- \frac{L}{n^3\pi^3}H_n\eta_0\left(1 - \delta(-1)^n\right)\sinh\left(\frac{2n\pi}{L}y\right)\right\},
\end{aligned} \tag{34}$$

with:

$$\begin{aligned}
H_0 =& \frac{\eta_0(\delta+1)L}{4\pi^2}, \\
H_1 =& \left(-\frac{1}{2} - 2\eta_0(1-\delta)\frac{L}{\pi^2} + 4\eta_0\frac{L}{\pi^2}\right)\operatorname{sech}\left(\frac{\pi}{L}\right), \\
H_n =& \frac{L^2}{n^2\pi^2}\eta_0\left(1 - \delta(-1)^n\right)\operatorname{sech}\left(\frac{n\pi}{L}\right), \\
K_n =& \left(D_n + \left(\frac{n}{\pi} + \frac{n(1-n)}{L}y\right)H_n + (1-n)E_n\right),
\end{aligned}$$

$$\begin{aligned}
F =& -\frac{1}{2\pi^2}\eta_0(\delta+1)\left(\frac{\pi}{L}C_1 - \frac{3}{2}H_1\right) + \frac{\pi}{8L}H_1 C_1 \\
&+ \sum_{n=2}^{\infty}\left\{\frac{1}{\pi^2}\eta_0\left(\delta(-1)^n - 1\right)H_n\left(\frac{\pi}{n}D_n + H_n - 2 + \frac{1}{n^2}\right)\right. \\
&\left.- \frac{1}{4}\frac{n^2}{L^2}H_n^2\left(\frac{1-n}{(n+1)^2} + \frac{1}{n-1}\right) - \frac{1}{2}\frac{n^3}{(n^2-1)L^2}\pi H_n D_n\right\},
\end{aligned}$$

$$
\begin{aligned}
G = &- \frac{L}{2\pi^2}\eta_0\,(\delta+1)\left\{\left(C_1 - 2\frac{L}{\pi}H_1\right)\sinh\left(\frac{\pi}{L}\right) + \left(C_2 + \frac{1}{2}H_1\right)\cosh\left(\frac{\pi}{L}\right)\right\} \\
&+ \frac{1}{16}H_1\left[\left(C_1 - \frac{L}{4\pi}H_1\right)\sinh\left(\frac{2\pi}{L}\right) + \left(C_2 + \frac{1}{2}H_1\right)\cosh\left(\frac{2\pi}{L}\right)\right] \\
&+ \sum_{n=2}^{\infty}\left\{\frac{L}{\pi^3}\eta_0\,(\delta(-1)^n - 1)\,H_n\left(\frac{\pi}{n}D_n + H_n - 2\right)\sinh\left(\frac{\pi}{L}\right)\right. \\
&+ \frac{L}{n\pi^2}\eta_0\,(\delta(-1)^n - 1)\left(E_n + \frac{n}{L}H_n\right)\cosh\left(\frac{\pi}{L}\right) \\
&+ \frac{1}{4}\frac{n}{L}H_nK_n\left(\frac{n}{(n+1)^2}\cosh\left(\frac{(n+1)\pi}{L}y\right) - \frac{n}{(n-1)^2}\cosh\left(\frac{(n-1)\pi}{L}y\right)\right) \\
&- \frac{1}{4\pi}\frac{n^2}{(n+1)^2L}H_n\left(2\frac{1-n}{n+1}H_n + \pi D_n\right)\sinh\left(\frac{2(n+1)\pi}{L}\right) \\
&- \frac{1}{4\pi}\frac{n^2}{(n-1)^2L}H_n\,(2H_n + \pi D_n)\sinh\left(\frac{2(n-1)\pi}{L}\right) \\
&\left.- \frac{L}{n^3\pi^3}H_n\eta_0\,(1 - \delta(-1)^n)\sinh\left(\frac{2n\pi}{L}\right)\right\} - F.
\end{aligned}
$$

At this point, we have obtained a complete set of solutions for (17) and (18) up to and including the first-order approximation. Note that as the Darcy-Rayleigh number is small, the asymptotic solutions are dominated by conduction. The behavior of thermal fluid flow will be significantly influenced by η_0. When $\eta_0 = 0$, the solution is similar to the one proposed by Daniels and Punpocha [28].

To investigate the solution of the governing Equations (10) – (11) for finite Darcy-Rayleigh number, we explore the numerical solution in the following section.

3.2. Numerical solution

Due to the non-linear term of Equation (11), a direct application of the finite-difference method will lead to a system of non-linear algebraic equations, which can consume many subsequent computational processes. Therefore, we shall follow the work of Daniels and Punpocha [28] and assign artificial time derivatives to obtain a numerical solution using a simple marching procedure in time. This method yields the parabolic governing equations in time as follows:

$$\frac{\partial\psi}{\partial t} = \frac{\partial^2\psi}{\partial x^2} + \frac{\partial^2\psi}{\partial y^2} + R\frac{\partial T}{\partial x}, \tag{35}$$

$$\frac{\partial T}{\partial t} = \frac{\partial^2 T}{\partial x^2} + \frac{\partial^2 T}{\partial y^2} - \frac{\partial\psi}{\partial y}\frac{\partial T}{\partial x} + \frac{\partial\psi}{\partial x}\frac{\partial T}{\partial y}. \tag{36}$$

The steady-state solution can be derived by setting $t \longrightarrow \infty$.

Using the forward difference scheme for the time derivatives and the central difference scheme for the spatial derivatives, the discrete form of Equations (35) – (36) are written as follows:

$$\psi_{i,j}^{n+1} = \psi_{i,j}^{n} + \frac{\Delta t}{\Delta x^2}\left(\psi_{i+1,j}^{n} - 2\psi_{i,j}^{n} + \psi_{i-1,j}^{n}\right) + \frac{\Delta t}{\Delta y^2}\left(\psi_{i,j+1}^{n} - 2\psi_{i,j}^{n} + \psi_{i,j-1}^{n}\right) + R\frac{\Delta t}{2\Delta x}\left(T_{i+1,j}^{n} - T_{i-1,j}^{n}\right), \tag{37}$$

$$T_{i,j}^{n+1} = T_{i,j}^{n} + \frac{\Delta t}{\Delta x^2}\left(T_{i+1,j}^{n} - 2T_{i,j}^{n} + T_{i-1,j}^{n}\right) + \frac{\Delta t}{\Delta y^2}\left(T_{i,j+1}^{n} - 2T_{i,j}^{n} + T_{i,j-1}^{n}\right) - \frac{\Delta t}{4\Delta x\Delta y}\left(\psi_{i,j+1}^{n} - \psi_{i,j-1}^{n}\right)\left(T_{i+1,j}^{n} - T_{i-1,j}^{n}\right) + \frac{\Delta t}{4\Delta x\Delta y}\left(\psi_{i+1,j}^{n} - \psi_{i-1,j}^{n}\right)\left(T_{i,j+1}^{n} - T_{i,j-1}^{n}\right). \tag{38}$$

As an initial condition, it is assumed that there is no flow inside the domain and heat is transferred only by conduction over the temperature on the upper boundary.

The numerical stability criterion for (37) and (38) is still open for discussion. However, for the problem at hand, we choose Δt to satisfy the following von Neumann stability criterion:

$$\Delta t \leq \frac{1}{2}\frac{\Delta x^2 \Delta y^2}{\Delta x^2 + \Delta y^2}. \tag{39}$$

This is similar to the work of Haque et al. [31]. Using (39), variables ψ and T are updated until the changes in ψ and T at any grid satisfy the following convergence criterion:

$$\left|(\psi, T)_{new} - (\psi, T)_{old}\right| \leq 10^{-8}.$$

The grid-independence and time-step sensitivity study are evaluated using the quantities of interest $\psi_{\max}$, $T_{center} = T(L/2, 1/2)$, and $Nu_{\max}$. Here, $\psi_{\max}$ denotes the maximum stream function within the computational domain and indicates the strength of the primary circulation. The quantity T_{center} represents the temperature at the cavity center and acts as a representative measure of the interior thermal field. The local Nusselt number Nu along the top wall is defined as:

$$Nu(x) = \left.\frac{\partial T}{\partial y}\right|_{y=1}.$$

The quantity $Nu_{\max}$ is the maximum local Nusselt number along the top wall and characterizes the peak local heat-transfer rate. Additionally, the relative differences reported in Table 1 are assessed with respect to the finest-grid solution,

Table 1. Grid-independence study for the rectangular cavity problem

Grid	$\psi_{\max}$	T_{center}	$Nu_{\max}$	Rel $\psi_{\max}$ (%)	Rel T_{center} (%)	Rel $Nu_{\max}$ (%)
41 x 41	0.000330695	0.499667	1.38143	0.119316	0.000894406	0.413074
61 x 61	0.000330916	0.499667	1.38567	0.0523048	0.000907783	0.107414
81 x 81	0.000331045	0.499668	1.3868	0.0136259	0.000671275	0.025952
101 x 101	0.00033109	0.499672	1.38716	0	0	0

using $\text{Rel}Q(\%) = |Q - Q_{\text{fine}}|/|Q_{\text{fine}}| \times 100\%$ where Q denotes the quantity under consideration and Q_{fine} is its value on the finest mesh.

Table 1 shows that the numerical solution effectively becomes independent of the grid as the mesh is refined from 41×41 to 101×101. The maximum stream function, $\psi_{\max}$, varies only slightly from 3.30695×10^{-4} to 3.31090×10^{-4}, with its relative difference decreasing from 0.1193% on the coarsest grid to zero on the finest one. Similarly, the cavity-center temperature, T_{center}, remains almost the same across all grids, changing only between 0.499667 and 0.499672, indicating very weak sensitivity to mesh refinement. The maximum Nusselt number, $Nu_{\max}$, shows a slightly larger variation, increasing from 1.38143 to 1.38716. However, its relative difference gradually decreases and reaches just 0.02595% on the 81×81 grid. These findings confirm the grid independence of the numerical solution, with the 81×81 mesh providing excellent accuracy and negligible deviation from the finest grid. Therefore, the 81×81 grid is used in subsequent simulations as an optimal balance between computational efficiency and numerical accuracy.

Table 2. Time-step sensitivity study for the rectangular cavity problem

Δt	Iterations	$\psi_{\max}$	T_{center}	$Nu_{\max}$	Rel $\psi_{\max}$ (%)	Rel T_{center} (%)	Rel $Nu_{\max}$ (%)
3×10^{-5}	51748	0.000331043	0.49986	1.3864	0.010359	0.0873	0.06847
2×10^{-5}	69412	0.000331043	0.49981	1.3865	0.010349	0.0777	0.0577
10^{-5}	110978	0.000331045	0.49967	1.3868	0.009912	0.0494	0.0360
5×10^{-6}	171391	0.000331077	0.49942	1.3873	0	0	0

Table 2 indicates that the numerical solution is only weakly influenced by the choice of time step within the range $\Delta t = 3 \times 10^{-5}$ to 5×10^{-6}. The maximum stream function, $\psi_{\max}$, remains nearly unchanged, with a maximum relative difference of 0.0104%. The cavity-center temperature, T_{center}, shows a slightly more noticeable variation, shifting from 0.49986 to 0.49942, but its maximum relative difference remains very small at only 0.0873%. Similarly, the maximum Nusselt number, $Nu_{\max}$, varies only slightly from 1.3864 to 1.3873, with its relative difference decreasing steadily as the time step decreases. As expected, the number of iterations increases significantly with smaller time steps, indicating a much higher computational cost. Overall, these findings confirm that the solution is effectively

independent of the time step, and $\Delta t = 10^{-5}$ is an appropriate choice, as it yields much better computational efficiency than the smallest time step.

Finally, to validate our numerical solutions, we compare our results with the analytical solutions (17) and (18). We took $L = 1$, $R = 0.01$, $\eta_0 = 0.1$, and $\delta = 1$. Comparing the values of ψ and T with analytical solutions, we find that the root mean square errors for all grids of ψ and T are as follows:

$$\epsilon_\psi = 1.1796 \times 10^{-6} \quad \text{and} \quad \epsilon_T = 3.1816 \times 10^{-4}. \tag{40}$$

Figure 2 shows sample plots comparing numerical and analytical solutions at three selected x values, namely $x = \frac{1}{4}$, $x = \frac{1}{2}$, and $x = \frac{3}{4}$.

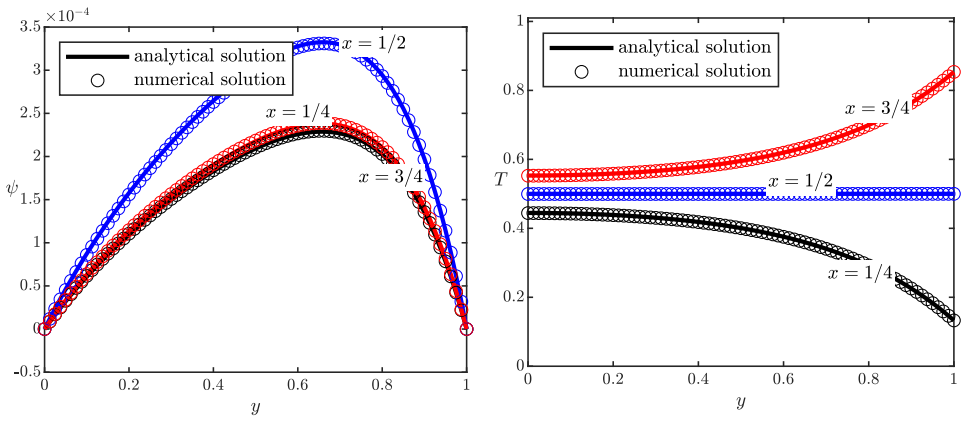

(a) ψ (b) T

Fig. 2. The numerical versus analytical solution at three selected positions: $x = \frac{1}{4}, \frac{1}{2}$, and $\frac{3}{4}$.

4. Results

This chapter discusses the numerical results for natural convection in a porous cavity with uniform heat flux on the side walls. The analysis is divided into three parts: first, comparing the current boundary condition with the classical insulated side-wall case to highlight the main differences in flow and temperature fields; second, investigating the impact of the side-wall heat-flux ratio parameter δ to understand how symmetric and asymmetric lateral heating influence overall thermal and hydrodynamic behavior; and third, examining the slip velocity and Nusselt number distributions along the cavity boundaries for deeper insight into local near-wall transport processes.

4.1. Comparison between insulated and uniform heat-flux side walls

As a baseline for the present analysis, the results for uniform heat-flux side walls are first compared with those for insulated side walls. This comparison aims to show how the side-wall thermal specifications affect flow intensity, temperature distribution, and overall heat transfer. Both qualitative and quantitative analyses are provided in this discussion.

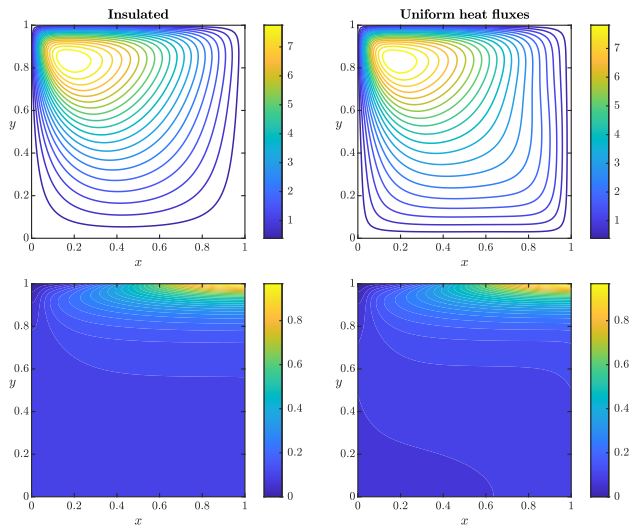

(a)

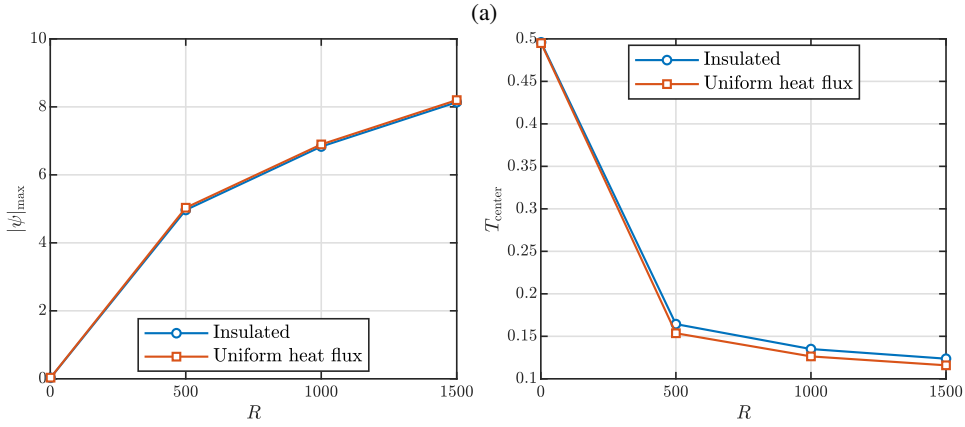

(b)

Fig. 3. Comparison between insulated and uniform heat-flux side walls for $\eta_0 = 0.1, \delta = 1, R = 1500$:
(a) streamlines and isotherms;
(b) variation of $|\psi_{\max}|$ and T_{center} with the Darcy-Rayleigh number R

Figure 3 presents both qualitative and quantitative comparisons between cases with insulated and uniform heat-flux side walls using $\eta_0 = 0.1$. The streamlines in Figure 3(a) reveal that the overall circulation pattern remains largely unchanged despite the different side-wall thermal boundary conditions. However, the isotherms clearly demonstrate a marked change in the temperature field, suggesting that the uniform heat-flux condition primarily impacts thermal distribution rather than the main flow pattern.

The graphs in Figure 3(b) confirm this finding quantitatively. The maximum stream functions are nearly identical in both cases across all R values, while the cavity-center temperature is always lower with uniform heat flux. Thus, the primary impact of setting the side-wall heat flux is a redistribution of heat within the cavity, with minimal effect on overall circulation strength. For practical porous enclosures, replacing insulated side-wall assumptions with uniform heat-flux conditions might not greatly change the predicted circulation strength. However, it can influence internal temperature and local thermal distribution. Consequently, if temperature uniformity or local thermal control is crucial, the side-wall thermal specifications should be considered.

After identifying the key differences between insulated and uniform heat-flux side-wall conditions, we then explore how changing the side-wall heat-flux ratio parameter, δ, affects the flow and thermal response.

4.2. Effect of the side-wall heat-flux ratio

The discussion now expands to include the impact of the heat-flux ratio parameter δ under uniform heat-flux side-wall conditions. Since δ governs the heat transfer ratio between the left and right walls, it significantly influences the cavity's thermal asymmetry. This subsection explores its effects on flow structure and temperature distribution.

In this simulation, we set a fixed value of $\eta_0 = 1$ and vary δ. Figure 4 shows streamlines and isotherms for a small Darcy-Rayleigh number and $L = 1$. Heat transfer primarily driven by conduction causes the thermal fluid to float near the upper surface, except when $\delta = 2$. A positive $\delta = 2$, indicating that heat is transferred into the domain through $x = 1$, causes the thermal fluid to float near the $x = 1$ (Figure 4[c]). Conversely, a negative δ signifies that heat is transferred from the cavity to the outside, shifting the hot fluid toward the right corner of the upper surface, and causing a double-cell circulation (Figure 4[b]).

Furthermore, taking the same size of cavity as before, we explore streamlines and isotherms for a large Darcy-Rayleigh number, as illustrated in Figure 5. A large Darcy-Rayleigh number induces thermal fluid motion in a convection mode. When $\delta = 0$ (Figure 5[a]), fluid flows around with two circulation centers. At $\delta = -2$, the circulation splits into multi-cell circulation (Figure 5[b]). The thermal boundary layer occurs when $\delta = 2$. However, the existence of heat flux tends to vanish

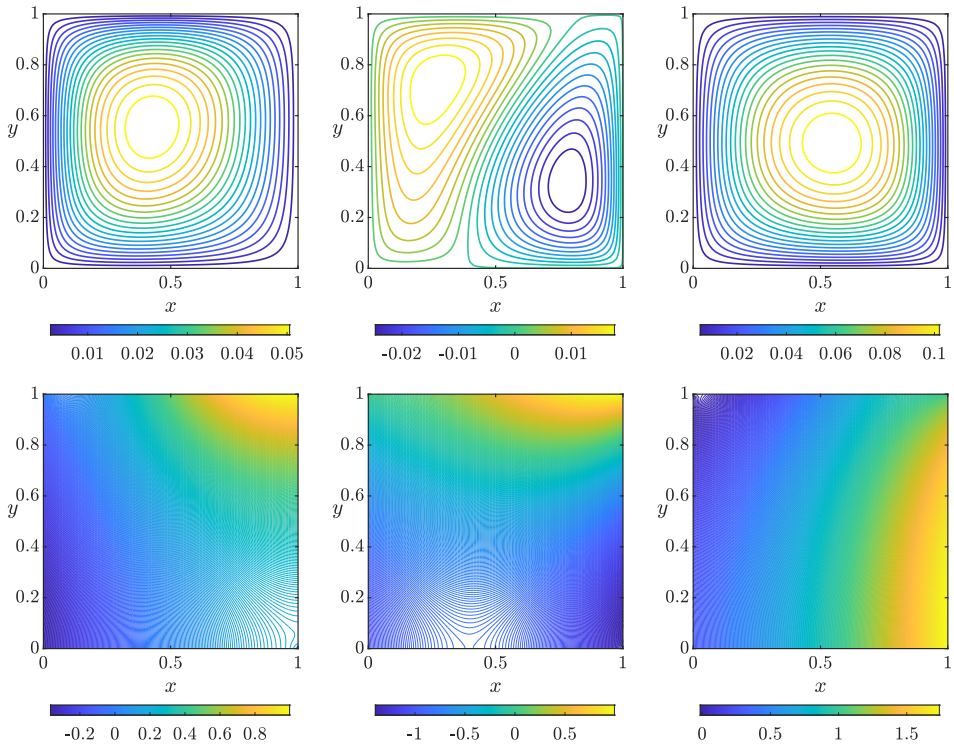

(a) $\delta = 0$ (b) $\delta = -2$ (c) $\delta = 2$

Fig. 4. Streamlines and isotherms for $R = 1$ and $\eta_0 = 1$ in a square cavity for various values of δ.

the thermal boundary layer near the upper surface, despite the fluid remaining in convection mode.

For further exploration, we present streamlines and isotherms for the tall and shallow cavities. Here, we set $\eta_0 = 1 = \delta$. These explorations describe the impact of cavity shape on fluid flow and heat transfer behavior. Figure 6 illustrates a cavity with $L = 4$ in relation to the shallow cavity. For a small Darcy-Rayleigh number, fluid flows symmetrically around $x = 2$ $(= L/2)$, and thermal fluid accumulates near the $x = 4$. For a large Darcy-Rayleigh number, the circulation center shifts toward the cold end of the upper surface. The tall cavity is depicted in Figure 7 with $L = 1/4$. The flow behavior aligns with that observed in a square cavity. However, a small gap between the two vertical walls leads to a significant heat-transfer effect, resulting in the absence of a thermal boundary layer.

4.3. Boundary distributions of slip velocity and Nusselt number

While earlier sections discussed the overall flow and thermal behavior of the cavity, a more detailed physical understanding can be gained by looking at the local transport along the boundaries. Specifically, the slip velocity and Nusselt number

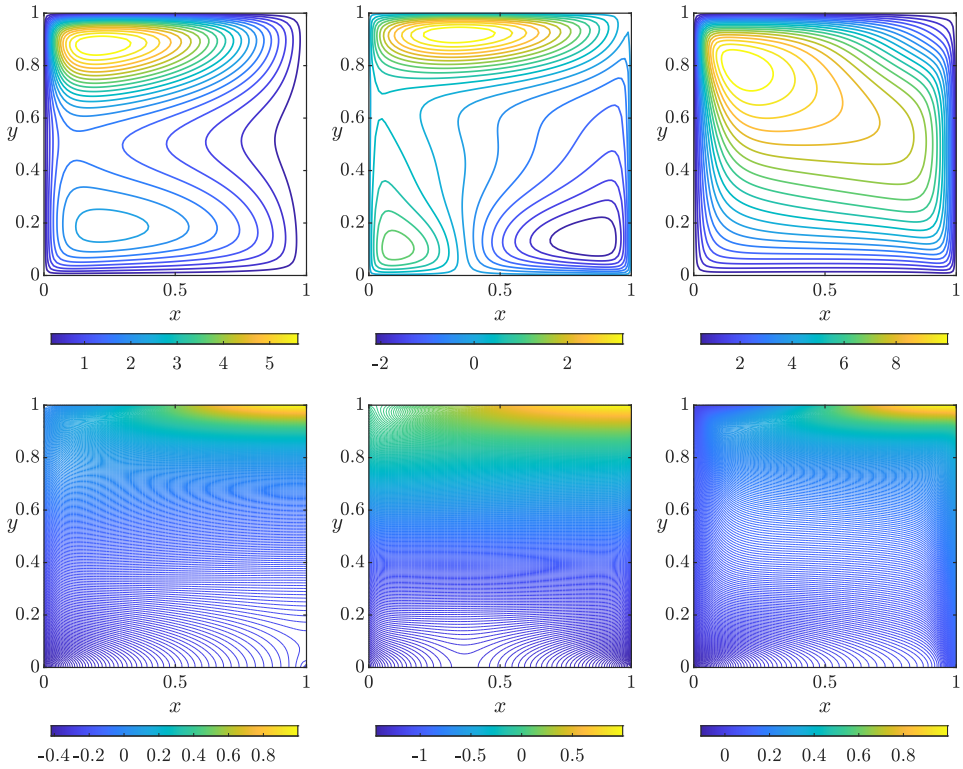

(a) $\delta = 0$ (b) $\delta = -2$ (c) $\delta = 2$

Fig. 5. Streamlines and isotherms for $R = 1500$ and $\eta_0 = 1$ in square cavity for various values of δ

distributions offer insights into the interaction between near-wall motion and heat transfer. This subsection explores how these boundary values change under uniform heat-flux conditions and how they reveal the flow and temperature structures inside the cavity. We illustrate slip velocities around the boundaries in Figure 8. We set $\eta_0 = \delta = L = 1$ and varying Darcy-Rayleigh number. This figure describes that although a non-slip condition is applied at the boundaries, the fluid exhibits a non-zero velocity relative to the walls. The larger the Darcy-Rayleigh number, the more significantly the convection influences the flow behavior. As the flow moves counterclockwise, velocities around the $x = 0$ and $y = 1$ walls become negative.

Equally important, we evaluate the overall heat-transfer efficiency of the cavity. The average Nusselt number is used as a comprehensive indicator of the wall heat-transfer rate. The average Nusselt number is then calculated by integrating the local Nusselt number along the entire top wall and dividing by the width of the cavity, and it can be expressed as follows:

$$Nu_{\text{Avg}} = \frac{1}{L}\int_0^L Nu(x)dx. \tag{41}$$

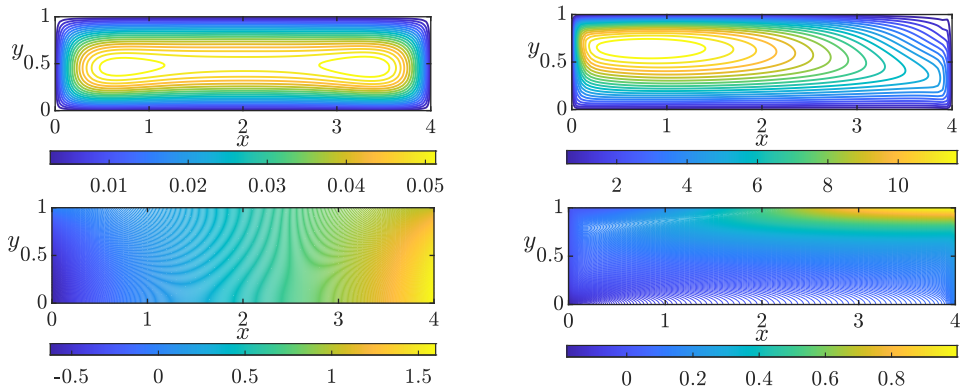

(a) $R = 1$ (b) $R = 1500$

Fig. 6. Streamline and isotherm in shallow cavity

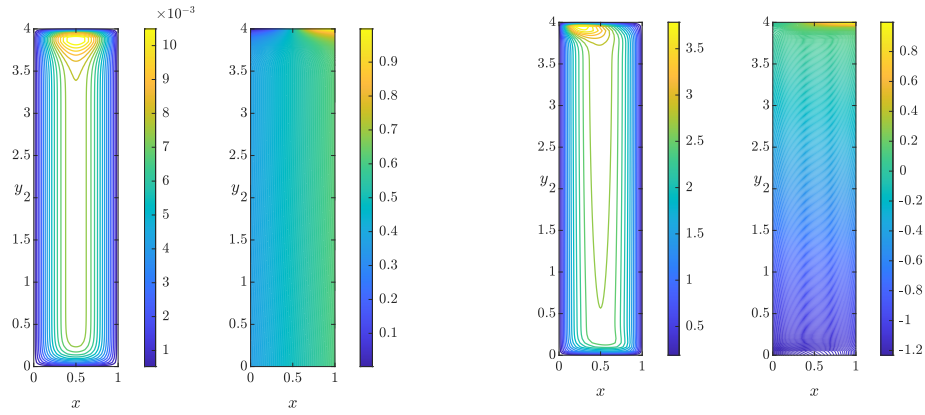

(a) $R = 1$ (b) $R = 1500$

Fig. 7. Streamline and isotherm in tall cavity

As shown in Figure 9, the average Nusselt number, Nu_{Avg}, steadily increases as R goes from 0 to 1500. At a small Darcy-Rayleigh number, Nu_{Avg} stays near zero, reflecting weak heat transfer and a regime mainly governed by conduction. As the Darcy-Rayleigh number increases, buoyancy-driven fluid motion intensifies, enhancing thermal mixing within the cavity and increasing the temperature gradient near the top wall. From an engineering perspective, this trend indicates that a higher Darcy-Rayleigh number leads to more efficient heat transfer through the top boundary and enhances the thermal performance of the cavity.

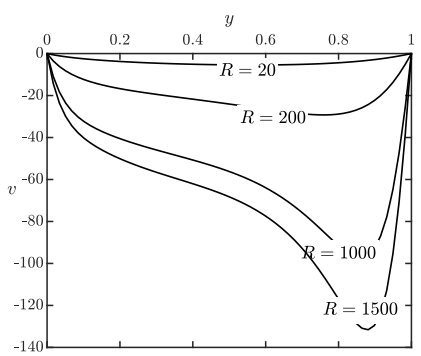

(a) around $x = 0$

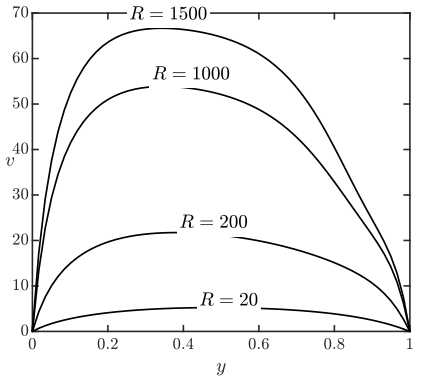

(b) around $x = 1$

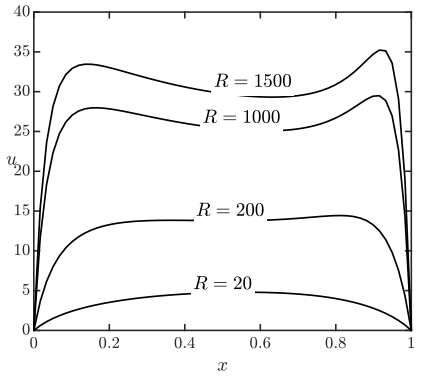

(c) around $y = 0$

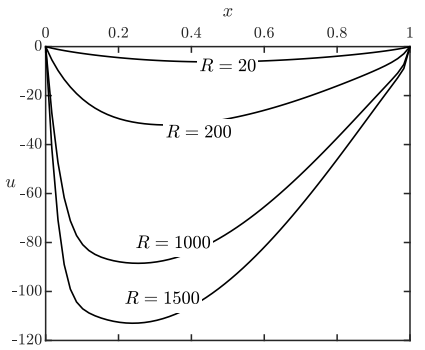

(d) around $y = 1$

Fig. 8. Slip velocity around the boundaries

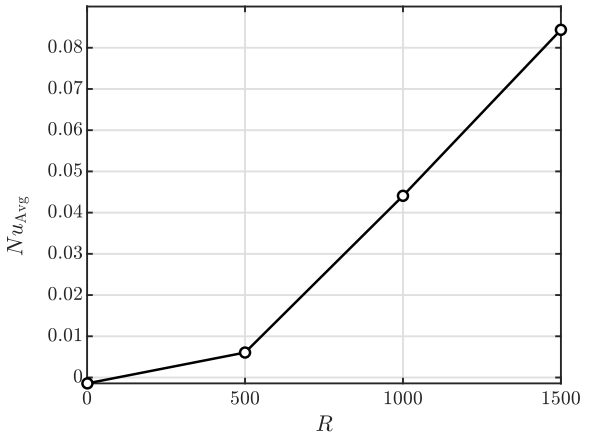

Fig. 9. The average Nusselt number with various R

5. Conclusions

In this paper, we studied the thermal fluid flow in a porous rectangular cavity driven by differential heating and uniform heat fluxes. We solved the governing equation analytically using the perturbation method by developing stream function and temperature variables based on the Darcy-Rayleigh number expansion. This analytical solution validated the numerical computation performed with the finite-difference method. Numerical simulations explored the thermal fluid flow behavior in the cavity. For zero heat fluxes, the streamlines and isotherms aligned with the findings presented by Daniels and Punpocha [28]. We also investigated heat transfer along one vertical side while thermally insulating the other. This condition created a double-cell circulation. The circulation developed into three corner rolls when both vertical sides had non-zero heat flux. Additionally, the flow behavior in shallow and tall cavities aligned with that observed in square cavities. However, in tall cavities, a small gap between the two vertical walls resulted in a significant heat-transfer effect because the reduced gap increased thermal confinement and modified the temperature gradients within the cavity. Finally, it should be noted that the present results were obtained within the framework of the classical Darcy model. Therefore, inertial corrections, such as Darcy-Forchheimer effects, may be relevant in more vigorous convection regimes and constitute a worthwhile extension of the present study.

Nomenclature

x_*, y_*	dimensional coordinates	k	thermal conductivity of the fluid-saturated porous medium
x, y	dimensionless coordinates	p_*	pressure
ℓ_x	cavity width	t	time
ℓ_y	cavity height	K	permeability of the porous medium
u_*, v_*	velocity components	g	gravitational acceleration
q_l	constant heat flux	R	Darcy-Rayleigh number
T_*	dimensional temperature	L	geometric aspect ratio
T	dimensionless temperature	Nu	Nusselt number
T_{0*}	reference temperature	$Nu_{\max}$	maximum Nusselt number
ΔT_*	temperature difference	Nu_{Avg}	average Nusselt number
$S(x_*/\ell_x)$	prescribed wall-temperature profile	T_{center}	temperature at the center of the cavity
$S(x/L)$	dimensionless wall-temperature profile		

Greek symbols

δ	heat-flux ratio of the vertical walls	η_0	dimensionless heat-flux parameter
μ	dynamic viscosity of the fluid	ψ_*	dimensional stream function
ρ	fluid density	ψ	dimensionless stream function
ρ_0	reference density	$\psi_{\max}$	maximum stream function
α	thermal diffusivity	ϵ_ψ	root-mean-square error of ψ
β	thermal expansion coefficient	ϵ_T	root-mean-square error of T

Acknowledgements

We would like to express our appreciation to The Ministry of Higher Education, Science, and Technology of the Republic of Indonesia, which has provided this research grant through The Penelitian Disertasi Doktor (grant number: 224/IT1.B07.1/SPP-LPPM/VI/2024). We also appreciate Beasiswa Pendidikan Indonesia managed by The Center for Higher Education Funding and Assessment, The Ministry of Higher Education, Science, and Technology of the Republic of Indonesia for providing a doctoral scholarship.

Author Contributions Conceptualization, R.R. and A.Y.G.; methodology, R.R. and A.Y.G.; validation, R.R., A.Y.G. and N.E.; data curation, R.R.; writing original draft preparation, R.R.; and writing, review, and editing, R.R., A.Y.G., and N.E. All authors have read and agreed to the published version of the manuscript.

Conflicts of Interest The authors declare that there are no conflicts of interest regarding the publication of this paper.

References

[1] L. Zhou, S.W. Armfield, N. Williamson, M.P. Kirkpatrick, and W. Lin, Natural convection in a cavity with time-dependent flux boundary, *International Journal of Heat and Fluid Flow*, 92:108887, Dec. 2021. doi: 10.1016/j.ijheatfluidflow.2021.108887.

[2] D.K. Singh and S.N. Singh, Conjugate free convection with surface radiation in open top cavity, *International Journal of Heat and Mass Transfer*, 89:444–453, Oct. 2015. doi: 10.1016/j.ijheatmasstransfer.2015.05.038.

[3] K.M. Shirvan, M. Mamourian, S. Mirzakhanlari, A.B. Rahimi, and R. Ellahi, Numerical study of surface radiation and combined natural convection heat transfer in a solar cavity receiver, *International Journal of Numerical Methods for Heat & Fluid Flow*, 27(10):2385–2399, Oct. 2017. doi: 10.1108/HFF-10-2016-0419.

[4] A. Bejan. *Convection Heat Transfer*. John Wiley & Sons, Hoboken, NJ, 2013.

[5] I.G.B. Darmawan, Rustandi, and Karyanto, Hydrothermal fluid flow modeling using numerical simulation to identify potential reservoir zones in the Mount Rajabasa geothermal field, *Kuwait Journal of Science*, 50(3):376–386, July 2023. doi: 10.1016/j.kjs.2023.02.025.

[6] S. Kang, J.Y. Choi, and S. Choi, Mechanism of heat transfer through porous media of inorganic intumescent coating in cone calorimeter testing, *Polymers*, 11(2):221, Jan. 2019. doi: 10.3390/polym11020221.

[7] C.G. Bankvall, Natural convection in vertical permeable space, *Wärme-und Stoffübertragung*, 7(1):22–30, Mar. 1974. doi: 10.1007/BF01438317.

[8] Y. Billaud, D. Saury, and D. Lemonnier, Numerical investigation of coupled natural convection and radiation in a differentially heated cubic cavity filled with humid air. Effects of the cavity size, *Numerical Heat Transfer, Part A: Applications*, 72(7):495–518, Oct. 2017. doi: 10.1080/10407782.2017.1386509.

[9] A. Lavrinenko, F. Gisbert, J. Pallares, and A. Fabregat, Fully-resolved numerical simulations of the turbulent flow and particle deposition in a cubical cavity with two pairs of differentially heated opposed walls at Rayleigh number 3.6×10^9, *International Communications in Heat and Mass Transfer*, 141:106564, 2023. doi: 10.1016/j.icheatmasstransfer.2022.106564.

[10] W.A. Hay and M.V. Papalexandris, Numerical simulations of turbulent thermal convection with a free-slip upper boundary, *Proceedings of the Royal Society A*, 475(2232):20190601, Dec. 2019. doi: 10.1098/rspa.2019.0601.

[11] F. Gao, D.B. Pitz, and J.W. Chew, Numerical investigation of buoyancy-induced flow in a sealed rapidly rotating disc cavity, *International Journal of Heat and Mass Transfer*, 147:118860, Feb. 2020. doi: 10.1016/j.ijheatmasstransfer.2019.118860.

[12] A. Rahimi, A.D. Saee, A. Kasaeipoor, and E.H. Malekshah, A comprehensive review on natural convection flow and heat transfer: the most practical geometries for engineering applications, *International Journal of Numerical Methods for Heat & Fluid Flow*, 29(3):834–877, Dec. 2019. doi: 10.1108/HFF-06-2018-0272.

[13] I. Hamzaoui, S. Millet, V. Botton, A. Benzaoui, D. Henry, L. Hachani, R. Boussaa, K. Zaidat, and Y. Fautrelle, A $2D^{1/2}$ model for natural convection and solidification in a narrow enclosure, *International Journal of Thermal Sciences*, 140:167–183, June 2019. doi: 10.1016/j.ijthermalsci.2019.02.028.

[14] V. Botton, R. Boussaa, R. Debacque, L. Hachani, K. Zaidat, H.B. Hadid, Y. Fautrelle, and D. Henry, A $2D^{1/2}$ model for low Prandtl number convection in an enclosure, *International Journal of Thermal Sciences*, 71:53–60, Sept. 2013. doi: 10.1016/j.ijthermalsci.2013.04.017.

[15] T. Yang, B. Wang, J. Wu, Z. Lu, and Q. Zhou, Horizontal convection in a rectangular enclosure driven by a linear temperature profile, *Applied Mathematics and Mechanics*, 42(8):1183–1190, July 2021. doi: 10.1007/s10483-021-2754-5.

[16] G.O. Hughes, and R.W. Griffiths, Horizontal convection, *Annu. Rev. Fluid Mech.*, 40(1):185–208, Jan. 2008. doi: 10.1146/annurev.fluid.40.111406.102148.

[17] J. Chery, A. Bonneville, J.P. Vilotte, and D. Yuen, Numerical modelling of caldera dynamical behaviour, *Geophysical Journal International*, 105(2):365–379, May 1991. doi: 10.1111/j.1365-246X.1991.tb06719.x.

[18] S. Chiu-Webster, E.J. Hinch, and J.R. Lister, Very viscous horizontal convection, *Journal of Fluid Mechanics*, 611:395–426, Sept. 2008. doi: 10.1017/S0022112008002942.

[19] D. Noto, H.N. Ulloa, T. Yanagisawa, and Y. Tasaka, Stratified horizontal convection, *Journal of Fluid Mechanics*, 970:A21, Aug. 2023. doi: 10.1017/jfm.2023.625.

[20] K.L. Walker and G.M. Homsy, Convection in a porous cavity, *Journal of Fluid Mechanics*, 87(3):449–474, Aug. 1978. doi: 10.1017/S0022112078001718.

[21] A. Bejan, On the boundary layer regime in a vertical enclosure filled with a porous medium, *Letters in Heat and Mass Transfer*, 6(2):93–102, Mar.–Apr. 1979. doi: 10.1016/0094-4548(79)90001-8.

[22] P.G. Daniels and M. Punpocha, On the boundary-layer structure of cavity flow in a porous medium driven by differential heating, *Journal of Fluid Mechanics*, 532:321–344, May 2005. doi: 10.1017/S0022112005004167.

[23] G.J. Sheard and M.P. King, Horizontal convection: effect of aspect ratio on Rayleigh number scaling and stability, *Applied Mathematical Modelling*, 35(4):1647–1655, Apr. 2011. doi: 10.1016/j.apm.2010.09.041.

[24] S. Hossain, T. Vo, and G.J. Sheard, Shallow enclosure horizontal convection: Insights from asymptotic expansion analysis, in Proc. *The 22nd Australasian Fluid Mechanics Conference (AFMC2020)*, Brisbane, Australia, 7–10 Dec. 2020. doi: 10.14264/06df42f.

[25] B. Yan and X. He, Transitional fluctuations of thermal boundary layer in horizontal convection, *International Journal of Heat and Mass Transfer*, 200:123542, Jan. 2023. doi: 10.1016/j.ijheatmasstransfer.2022.123542.

[26] T. Tsai, W.K. Hussam, M.P. King, and G.J. Sheard, Transitions and scaling in horizontal convection driven by different temperature profiles, *International Journal of Thermal Sciences*, 148:106166, Feb. 2020. doi: 10.1016/j.ijthermalsci.2019.106166.

[27] P.G. Daniels, On the boundary layer structure of differentially heated cavity flow in a stably stratified porous medium, *Journal of Fluid Mechanics*, 586:347–370, Aug. 2007. doi: 10.1017/S0022112007007100.

[28] P.G. Daniels and M. Punpocha, Cavity flow in a porous medium driven by differential heating, *International Journal of Heat and Mass Transfer*, 47(14-16):3017–3030, July 2004. doi: 10.1016/j.ijheatmasstransfer.2004.03.004.

[29] A. Bejan, The boundary layer regime in a porous layer with uniform heat flux from the side, *International Journal of Heat and Mass Transfer*, 26(9):1339–1346, Sept. 1983. doi: 10.1016/S0017-9310(83)80065-9.

[30] J. Li, Y. Yang, and C. Sun, From Darcy convection to free-fluid convection: pore-scale study of density-driven currents in porous media, *Journal of Fluid Mechanics*, 1009:A10, Apr. 2025. doi: 10.1017/jfm.2025.213.

[31] M.N. Haque, R. Akter, and M.S.H. Mojumder, An Efficient Explicit Scheme for Solving the 2D Heat Equation with Stability and Convergence Analysis, *Journal of Applied Mathematics and Physics*, 13(7):2234–2244, June 2025. doi: 10.4236/jamp.2025.137127.